Research Square

Preprints are preliminary reports that have not undergone peer review.
They should not be considered conclusive, used to inform clinical practice,
or referenced by the media as validated information.

Impact of topography and land cover on air temperature space-time variability in an urban environment with contrasted topography (Dijon, France, 2014–2021)

Julien Crétat (julien.cretat@u-bourgogne.fr)
University of Burgundy
Yves Richard
University of Burgundy
Benjamin Pohl
University of Burgundy
Justin Emery
University of Burgundy
Julita Dudek
University of Burgundy
Damien Roy
University of Franche-Comté
Julien Pergaud
University of Burgundy
Mario Rega
University of Burgundy
Mélissa Poupelin
University of Burgundy
Daniel Joly
University of Franche-Comté
Thomas Thévenin
University of Burgundy
Eva Marquès
Centre National de Recherches Météorologiques
Valéry Masson
Centre National de Recherches Météorologiques

Research Article

Keywords: MUSTARDijon, linear regression, topography, land cover, urban heat island, thermal inversion, adiabatic gradient

Posted Date: March 6th, 2023

DOI: https://doi.org/10.21203/rs.3.rs-2620006/v1

License: This work is licensed under a Creative Commons Attribution 4.0 International License. Read Full License

Additional Declarations: No competing interests reported.

Version of Record: A version of this preprint was published at Theoretical and Applied Climatology on November 18th, 2023. See the published version at https://doi.org/10.1007/s00704-023-04742-4.

Abstract

The influence of topography and land cover on air temperature space-time variability is examined in an urban environment with contrasted topography through simple and multiple linear regression (SLR and MLR) models ran for each hour of the period 2014–202 to explain air temperature spatial patterns observed by a dense in-situ network.

The SLR models reveal a complementary influence of topography and land cover, with largest influence during daytime and nighttime, respectively. The MLR significantly improves upon the SLR models despite persistent intensity errors at night and spatial errors in the early morning. Topography influences air temperatures all year round, with an adiabatic gradient during the day and frequent thermal inversions at night (up to 30% of the time). Impervious surfaces are more influential in summer and early fall, especially during the late afternoon for the fraction covered by buildings, and during the early night for distance from the city centre. They contribute to warm air temperature close to the city centre and where the fraction covered by buildings increases. On the other hand, vegetation contributes to cool air temperature during the night, especially in spring and early summer for field crops, summer and early fall for forests and water, and late fall and winter for low vegetation.

Our framework proves to be a low-cost and efficient way to understand the static drivers of air temperature along the annual and diurnal cycles, and is easily transposable to other areas and study fields, such as viticultural environments to further understand spring frost events.

1. Introduction

There is growing interest for understanding air temperature space-time variability in urban environments, because cities are highly vulnerable to climate change and are home for about 60% of the world's population — a percentage expected to reach 70% by 2050 according to the (United Nations 2019). The most popular phenomena under study are the so-called Urban Heat Islands (UHIs). UHIs correspond to a well-known mechanism inducing warmer surface and air temperature over urban than adjacent rural areas, due to sensible heat absorption and storage by mineral surfaces and buildings, and weak evapotranspiration of impervious surfaces (Oke 1973, 1982; Oke et al. 2017). UHIs exacerbate human thermal stress in summer, especially during heat waves and hot spells (Fouillet et al. 2006; Matzarakis et al. 2009; Gabriel and Endlicher 2011; Steeneveld et al. 2011; Pascal et al. 2018), but may also be an opportunity to reduce energy consumption (Li et al. 2019) and cold-related mortality during winter compared to adjacent rural areas (Macintyre et al. 2021).

Many previous studies dedicated to assess the drivers of urban air temperature variability have focused on UHIs and compared individual effects through correlation and regression analyses. This has been done considering individual factors (Oke 1973; Jusuf et al. 2007; Imhoff et al. 2010; Tan and Li 2015) and more rarely multiple factors (Peng et al. 2012; Coseo and Larsen 2014; Wang et al. 2021). The UHI intensity increases proportionally to the size and population of the urban area (Oke 1973) and under calm

(wind speed < 2 m/s), clear-sky and dry-air conditions (Oke 1982; Morris et al. 2001; Mestayer et al. 2005; Hoffmann and Schlünzen 2013; Arnds et al. 2017). UHIs also tend also to intensify under thermal inversions even in relatively flat cities (Oke and Maxwell 1975; Nkemdirim 1980; Goldreich 1984; Kuttler et al. 1996; Szymanowski 2005; Hidalgo et al. 2010; Bokwa et al. 2015). Elevation and landforms have been shown to modulate UHIs, with e.g. air temperature cooling with elevation during the day and colder conditions on northern than southern slopes (Zhao et al. 2016; Peng et al. 2020). In addition, landforms significantly affect air temperature spatial patterns (Geiger et al. 2003; Whiteman et al. 2004). At the end of the night, cold air tends to slide downslope and accumulate in the valley bottoms (katabatic wind) while the hilltops and upper slopes experience milder temperatures. Conversely, in the middle of the day, warm air is further heated by contact with the ground and tends to rise along hillslopes exposed to the sun (anabatic wind). These landform-induced thermal effects, also known as slope breezes, influence air temperature well beyond the hillslopes where they are generated. Finally, land cover affects the surface energy and radiation balance (Oke 1982) and can lead to marked air temperature contrasts both within cities, but also between them and the surrounding rural environment. Mineral surfaces tend for instance to slow nighttime cooling (Eliasson 1996), unlike plant-covered surfaces that cool more rapidly (Sun et al. 2009; Sun 2011; Heusinkveld et al. 2014; Song et al. 2014). Green areas form Urban Cool Islands (UCIs), which can contribute to cool air temperature 300 to 1000 m beyond them (Petralli et al. 2014). City centres are not systematically the hottest parts of town due to local shading and canyon effect (Hart and Sailor 2009; Sun et al. 2009).

The assessment of topography and land cover effects on air temperature space-time variability has been facilitated thanks to the development of fine-scale digital terrain models and vectorial database describing land cover at high spatial resolution. These effects vary over both annual and diurnal cycles (e.g. Fenner et al. 2014; Wicki and Parlow 2017; Nikoloudakis et al. 2020) and are modulated by climatological and meteorological conditions (Johnson et al. 1991; Alcoforado and Andrade 2006; Heusinkveld et al. 2014), thereby suggesting potential antagonist effects depending on the time of day and year. Furthermore, an accurate assessment of the drivers of urban air temperature variability requires to sample air temperature at high spatial resolution over a long time period (e.g., multiple years) to account for (i) the diversity of land cover and topographical properties within and around the city, (ii) huge air temperature amplitude along the annual and diurnal cycles and (iii) internal variability of the climate system. To date, very few networks fulfil this requirement. In France, for instance, two cities only are equipped with a dense network recording air temperature for 10 years or so (Rennes and Dijon).

This paper explores the individual and combined influences of topography and land cover on air temperature space-time variability as measured in Dijon, France, by a dense station network (up to 67 sites) from 2014 to 2021. We build over previous studies by applying Simple and Multiple Linear Regression (SLR/MLR) analyses to examine the individual and combined effects of topography and land cover on air temperature spatial patterns along both the annual and diurnal cycles. The originality of the approach is twofold. First, the regression approach is not used in a predictive mode (e.g., one unique or few SLR/MLR models) but as a framework to objectively identify the individual factors and their combination explaining each air temperature spatial pattern. This implies one SLR/MLR model to be built

for each hour for the period 2014–2021. Second, in addition to traditional metrics used to assess individual and combined influences (e.g., root mean square error and coefficient of determination), we also examine the frequency of occurrence and mean regression coefficient associated with SLR and MLR predictors along the annual and diurnal cycles to pinpoint when and how they influence air temperature spatial patterns.

The paper is organized as follows. Section 2 presents the site area, the data and the SLR and MLR frameworks. Section 3 presents both the individual and combined influences of the predictors in the SLR and MLR frameworks, respectively. Section 4 gives the main conclusions and discusses the limitations of our work.

2. Material And Methods

2.1 Site area

The study area is Dijon located in Burgundy, eastern France. Dijon is a mid-sized European city of about 260 000 inhabitants that covers 240 km^2 (Fig. 1). The city is bordered to the west by a ~ 500 m plateau (Fig. 2a-c) that is largely forested (Fig. 2g). This plateau is incised by a steep-sided valley (Fig. 2a-c) that is mostly grassland (Fig. 2i). The ~ 220 m plain lying east of the city (Fig. 2a-c) is covered by field crops (Fig. 2h), forests and ponds further east (Fig. 2i). The city is characterized by three main built-type categories forming a concentric pattern: compact mid-rise in the city centre and compact low- and high-rise further from the city centre (Emery et al. 2021). Forests and low vegetation are sparse within the city, except for in a 33 ha urban park some 3 km south-east of the city centre, around a 37 ha lake in the western part of the city, and beside the River Ouche (Fig. 2g, i) that flows through the city from northwest to southeast (Fig. 1).

Dijon is characterized by a Köppen temperate oceanic climate (Cfb) on the European scale and by a continental-like climate on the French scale (Joly et al. 2010). The climatological conditions, derived from the Météo-France weather station located south-east of the city (blue dot in Fig. 1), are characterized by wide variability in diurnal temperatures and insolation over the annual cycle, with relatively hot summers and cold winters (Fig. 3a-b). This contrasts with rainfall amounts, which vary barely over the mean diurnal and annual cycles (Fig. 3c). Rainfall amounts seem to be slightly higher in the late afternoon when convective precipitation dominates (April to July: see Marteau et al. 2015), and at night when stratiform precipitation prevails (November to February: ibid.). Wind speeds display a somewhat insubstantial annual cycle, but a prominent diurnal cycle showing higher speeds during the day (Fig. 3d). At night, south-westerlies dominate during winter and north-westerlies dominate during the remaining seasons (Fig. 3e-f). Wind direction varies a lot during the day, hence weak climatological values (Fig. 3e-f.)

2.2 Data

2.2.1 Hourly air temperature measurements

Hourly air temperatures come from the MUSTARDijon network (Richard et al. 2018; Fig. 1). The network has been designed to capture mesoscale rather than local or microscale thermal conditions (Oke 1984, 2006) over the various land cover categories found in Dijon. The network is equipped with sensors measuring near instantaneous temperatures every hour at 3 m above ground level since 6 June 2014. The network has been progressively densified from 50 sensors in 2014 to 67 in 2021 (Fig. 1). Until 2019, air temperatures were measured with HOBO Pro v2 U23-001A sensors, which were accurate to ± 0.25°C from − 40 to 0°C and ± 0.2°C from 0 to 70°C, and measurements were collected manually, once a year. These sensors were replaced by automatic HOBO MicroRX stations equipped with HOBO S-THC-M002 sensors between 2020 and 2021 (Fig. 1). The new sensors have a similar accuracy but their response time is shorter (~ 4 minutes compared to ~ 10 minutes for the previous sensors). This induces slightly more pronounced air temperature variability when measured by the newer sensors, but these changes do not significantly impact our results. The period studied runs from 6 June 2014 to 31 December 2021, with ~ 3.5% missing values due to sensor failure/maintenance.

2.2.2 Topography and land cover descriptors

Three categories are used as potential predictors to explain observed air temperature space-time variability at the hourly timescale: (i) topography, (ii) distance from the city centre and (iii) land cover (Fig. 2).

Topography descriptors are derived using the 50 m resolution Digital Terrain Model (DTM) from the Institut Géographique National (IGN). We consider the elevation of the closest 50 m pixel for each sensor (Fig. 2a and Table 1) since elevation drives a west–east gradient in air temperature across Dijon (Richard et al. 2018). Landform effects are accounted for by considering the magnitude of humps and of valleys (Fig. 2b-c), which characterize the height or depth of a positive or a negative relief relative to a topographic reference point. Following Joly et al. (2012), the magnitude of humps and valleys has been computed in three stages. First, ridgelines and thalwegs have been identified using the Peucker and Douglas (1975) algorithm applied to the DTM elevation spatially averaged considering 7 50 m pixels. The spatial averaging of 7 pixels allows to focus on the most prominent ridgelines and thalwegs, which would have been too noisy using 5 pixels and too smoothed using 9 pixels (Supplementary Fig. S1). Second, we have constructed two fictitious topographic surfaces: (1) the “ceiling” passing through all the ridgelines to encompass all of the emerging relief and (2) the “floor” joining up all the thalwegs. Between these two surfaces, the distance varies locally with the altitudinal position of the ridgelines relative to the thalwegs. The ridgelines and thalwegs, often separated by great distances, depict surfaces with a long radius of action. Finally, the hump magnitude is obtained by the difference between the altitude of the floor vertically below pixel *p* and the elevation of the same pixel *p* provided by the DTM. The valley magnitude is the difference between the altitude of the ceiling vertically above pixel *p* and the altitude of pixel *p*.

	Predictor	Definition
Tendency term	Distance from the city centre (m)	Euclidean distance between each station and the city centre (Libération square)
Land cover	Fraction of buildings (%)	Fraction computed on 300 m circular buffer around each station
	Fraction of forests and water (%)	
	Fraction of field crops (%)	
	Fraction of low vegetation (%)	
Topography	Elevation (m)	closest 50 m pixel
Land form	Hump magnitude (m)	average of the 7 closest 50 m pixels
	Valley magnitude (m)	

Table 1: Predictors used as independent variables in the simple and multiple linear regression (SLR and MLR, respectively) models to explain hourly air temperature patterns measured by the MUSTARDijon network (dependent variable). The SLR models are fed by each of the 8 predictors listed in column 2. The MLR models are fed by 5 predictors at most out of the 6 groups of predictors, coloured in grey scale in column 2. They never uses either distance from the city centre and the fraction of buildings, or elevation and hump magnitude at the same time to avoid multicollinearity issues.

The distance from the city centre is an isotropic tendency term which implicitly describes the decrease in urban density (resulting therefore in a similar decrease in impervious surfaces) with distance from the city centre (Fig. 2d). This tendency term is known to affect air temperature spatial patterns in urban environments (Edmondson et al. 2016) and is computed as the Euclidean distance between each station and the city centre (Libération square: black cross in Fig. 1).

Land cover descriptors have been derived using a hybrid product mixing the French BD TOPO database (version 2, 2020) developed by IGN and one satellite image from Pléaides acquired in August 2015 at 2 m resolution. The BD TOPO2 is preferred to other products (e.g. MAPuCE; Bocher et al. 2018) for consistency with other projects in which our team is currently involved. Vegetation in BD TOPO2 is obtained by automatic classification using supervised learning followed by a series of processing operations during which the unwooded vegetation-covered surfaces are removed (e.g., meadows and grasslands) for polygons of less than 50 ares (i.e., 5000 m^2). The Pléiades image is used to make up for this missing information by calculating the modified soil-adjusted vegetation index (MSAVI version 2: Qi et al., 1994) based on the red (590 to 710 nm) and near infrared (740 to 940 nm) spectral bands (Eq. 1).

$$MSAVI2 = \frac{2\times NIR+1-\sqrt{(2\times NIR+1)^2-8\times(NIR-RED)}}{2} \quad \text{Eq. (1)}$$

The MSAVI2 is an index designed to substitute the normalized difference vegetation index (NDVI) where it fails to provide accurate data due to low vegetation or a lake of chlorophyll in the plants (Qi et al. 1994). It improves on the NDVI by incorporating a soil adjustment factor into the denominator of the NDVI

equation. The incorporation of soil-adjusted indices greatly improves vegetation models (Bannari et al. 2000). This factor varies inversely with the amount of vegetation present, which increases the dynamic range of the vegetation signal while further minimizing the soil background influences (Qi et al. 1994).

The BD TOPO2 – Pléiades hybrid product is used to derive the area fraction covered by (i) buildings (Fig. 2e), (ii) artificial surfaces (buildings and transport infrastructures; Fig. 2f), (iii) forests and water (Fig. 2g), (iv) field crops (Fig. 2h) and (v) low vegetation (Fig. 2i). Following Foissard et al. (2019), these descriptors have been computed within a circular buffer of 50m to 600m radius, every 50m, and around each sensor, to assess the impact of the buffer size on air temperature spatial variability. The impact of the buffer size is weak for the fraction covered by buildings and field crops but is non-negligible for the fraction covered by forests and water and by low vegetation (Supplementary Fig. S2). Among the buffer size tested, a 300m radius leads to satisfactory results for all land cover descriptors, and is thus retained in this study. Thus, the total area fraction covered by artificial surfaces and the three vegetation categories equals 100%, a necessary step guaranteeing there is no loss of information and no overlapping information in our BD TOPO2 – Pléiades hybrid product. Importantly, this product gives an instantaneous view of land cover, which is by no means perfect since we use it to assess its impacts on air temperature spatial patterns for the period 2014–2021. However, land cover properties did not drastically change around the sensors during this period, allowing us to use static land cover descriptors with confidence.

To limit information redundancies, the collinearity between the above-described descriptors has been examined (Supplementary Fig. S3). Four couples of descriptors depict strong collinearities: (i) elevation and hump magnitude (r = 0.87), (ii) distance from the city centre and fraction of buildings (r=-0.71), (iii) fraction of buildings and artificial surfaces (r = 0.66), and (iv) fraction of artificial surfaces and field crops (r=-0.62). Based on these results, we decided to exclude artificial surfaces from the analyses since this descriptor is significantly correlated with many others (Supplementary Fig. S3). On the other hand, we opted to keep the best predictor (based on *p* values) between elevation and hump magnitude and between the distance from the city centre and the fraction covered by buildings when assessing the combined effects of the predictors. The exact list of predictors mobilized in this study and the way they are computed are summarized in Table 1.

2.3 Assessing individual and combined influences of topography and land cover on air temperature space-time variability

Individual and combined influences of the above-described descriptors on air temperature space-time variability are assessed using simple and multiple linear regression (SLR and MLR) frameworks, respectively. In both cases, the aim is not to build a predictive model for air temperature, but to assess the individual and combined influences of the predictors in terms of frequency of occurrence and thermal effect (i.e., regression coefficient) without imposing subjectively the nature and number of predictors for MLR models.

To do so, we have constructed one SLR/MLR model for each hour of the period 2014–2021 when at least 40 sensors have no missing values. Each SLR model is built with each of the eight predictors listed in Table 1, regardless of the statistical significance of its influence. This leads to 66 347 SLR models for each predictor out of the 66 386 hourly timesteps of the period.

Slightly less MLR models are built (66 289) because, unlike the SLR models, they account for the statistical significance of the predictors. Each MLR model is built as a combination of 1 to 5 out of 6 potential predictors (Table 1: distance from the city centre or fraction of buildings, fraction of forests and water, field crops and low vegetation, elevation or hump magnitude and valley magnitude). Retaining 5 predictors at most is the best compromise between MLR skill and MLR complexity (Supplementary Fig. S4). The number and ranking of predictors used to build each MLR model are chosen objectively based on *p* value at the 95% confidence level, implying that the number and nature of predictors feeding the MLR models are not fixed in time (even between two successive hours). Out of the 66 289 MLR models built for the period 2014–2021, 16% use 5 predictors, 23% 4 predictors, 35% 3 predictors, 22% 2 predictors and 4% only are based on SLR (with 1 predictor). In all cases, the predictors used to build the MLR models weakly co-vary when two or more predictors are used as inputs. The variance inflation factor remains below 2 more than 90% of the time and is almost always below 5 (Table 2), indicating weak multicollinearity issues (Craney and Surles 2002; James et al. 2017).

Table 2
Key statistics of the Variance Inflation Factor (VIF) computed for each MLR model set with 5 predictors at most for the period 2014–2021.

Predictor name	Min VIF	Max VIF	Mean VIF	Frequency of VIF < 2 (%)	Frequency of VIF < 5 (%)
Distance from the city centre	1.00	2.69	1.46	91.67	100.00
Fraction of buildings	1.00	6.99	1.36	92.82	99.73
Fraction of forests and water	1.00	4.12	1.43	94.30	100.00
Fraction of field crops	1.00	5.37	1.64	92.93	99.96
Fraction of low vegetation	1.00	2.32	1.23	99.75	100.00
Elevation	1.00	2.13	1.17	99.99	100.00
Hump magnitude	1.00	2.04	1.18	99.93	100.00
Valley magnitude	1.00	1.37	1.11	100.00	100.00

2.4 Statistical analyses

The individual and combined influences of topography and land cover on air temperature space-time variability is assessed by examining SLR/MLR skill metrics, as well as the frequency of occurrence of the predictors and their regression coefficients.

Two skill metrics are considered. First, the root mean square error (RMSE), computed for each sensor using a leave-one-out cross validation (LOOCV) then area-averaged, gives insights on the SLR/MLR capability in capturing the observed air temperature magnitude across the city. Second, the coefficient of determination (R2) for SLR models and adjusted R2 (R2-Adj) for MLR models, computed for all sensors at a time, assess the SLR/MLR capability in capturing the observed air temperature spatial patterns. These two metrics give complementary information (magnitude and spatial errors, respectively) and are used to hierarchy the individual (SLR models) effects of topography and land cover on air temperature space-time variability and discuss the extent to which MLR models improves on SLR models.

The frequency of occurrence of the predictors is examined in three different ways. First, we analyse the frequency of occurrence of SLR-derived positive/negative regression coefficients over the annual and diurnal cycles, to discuss the stationarity in the thermal effects of these predictors. Second, we compute the frequency of occurrence of each MLR-derived predictor as the ratio between the number of times it is selected in the MLR models at a given hour of a given month for the period 2014–2021 (nominator), and the total number of predictors used for the same hour, month and period (denominator). Third, we compute the frequency of occurrence of each predictor as the ratio between the number of times it enters the MLR models for each hour and month for the period 2014–2021 (nominator), and its total occurrence all months and days combined for the same period (denominator). This ratio is then compared to equiprobable occurrence along the annual and diurnal cycles (1/288, with 288 = 12 months x 24 hours) to pinpoint when the predictors are more (positive values) or less (negative values) frequent than expected. The difference between real and equiprobable distributions is tested using a Chi-2 test. This way to compute the frequency of occurrence allows assessing when each MLR-derived predictor preferentially occurs over both the annual and diurnal cycles.

The SLR- and MLR-derived regression coefficients describe the thermal effect of each predictor, i.e. whether a given predictor contributes to warm or to cool air temperature in the SLR/MLR frameworks. We examine both the probability density function of SLR-derived regression coefficients and the mean MLR-derived values along the annual and diurnal cycles to qualitatively assess the thermal effect of topography and land cover.

3. Results

3.1 Individual effects

Individual effects are assessed by analysing the results from the SLR models built for each hour of the period 2014–2021 and fed by each predictor listed in Table 1.

3.1.1 Hierarchizing the predictor's influence

Figures 4 and 5 show, for each predictor, the SLR-derived RMSE and R2 along both the diurnal and annual cycles, respectively. The mean RMSE are relatively similar for all predictors (Fig. 4). They are the lowest in the early morning (0.3°C to 0.5°C), increase during the day and reach their largest values during the night (0.7°C to 1°C). Such a diurnal cycle in the RMSE is less marked in fall and winter than in spring and summer, i.e. when air temperature and insolation are the lowest (Fig. 3a-b).

Spatial errors depend on the predictor feeding the SLR models. Four out of the eight predictors contribute to explain a significant fraction of air temperature spatial patterns: (1) elevation and (2) hump magnitude during daytime, especially in the late afternoon (R2 up to 0.9 and 0.6, respectively); (3) distance from the city centre and (4) fraction covered by buildings during nighttime (R2 up to 0.5). The remaining predictors have a much lower influence, with R2 values never exceeding 0.2 during nighttime and rarely exceeding 0.1 during daytime. These results suggest complementary influences of topography and land cover throughout the diurnal cycle, hence the need to account for both of them to capture observed air temperature space-time variability.

3.1.2 Thermal effects

Individual thermal effects are examined by analysing both the frequency of occurrence of SLR-derived regression coefficients (i.e., slopes of the SLR models) according to their sign (Table 3 and Fig. 6) and the probability density function of regression coefficients (Fig. 7). Topography and landform predictors are associated with regression coefficients that significantly vary in sign with time (Table 3). The regression coefficients are negative 80% of the time and positive 20% of the time for both elevation and hump magnitude, indicative of much more frequent adiabatic gradient than thermal inversion conditions.

Table 3
Frequency of occurrence (%) of SLM-derived regression coefficients (i.e., slopes) associated with positive and negative values for the period 2014–2021.

Predictors	Positive regression coefficient	Negative regression coefficient
Distance from the city centre	6.4	93.6
Fraction of buildings	97.2	2.8
Fraction of forests and water	8.4	91.6
Fraction of field crops	9.1	90.9
Fraction of low vegetation	5.2	94.8
Elevation	18.3	81.7
Hump magnitude	18.3	81.7
Valley magnitude	34.4	65.6

Adiabatic gradients are almost systematic during daytime (Fig. 6a-b) with a modal value of -0.9°C/100m for elevation (Fig. 7a) and − 0.3°C/10m for hump magnitude. They are also frequent during nighttime (70% of the time: Fig. 6a-b), albeit their slightly weaker magnitude (Fig. 7a-b). Symmetrically, thermal inversions are rare during daytime while occur up to 30% of the time during nighttime (Fig. 6a-b). They can reach up to 2°C/100m for elevation and 0.7°C/10m for hump magnitude, against maximal values of -1.5°C/100m and − 0.5°C/10m in the case of adiabatic gradients (Fig. 7a-b). Valley magnitude is associated with regression coefficients that are positive 35% of the time (and thus negative 65% of the time: Table 3). For this predictor, negative regression coefficients denote colder air temperature in than out of the valleys, which can result from different mechanisms including e.g. thermal inversions during nighttime or lower insolation in incised valleys than plateaus and plains during daytime. Such a configuration is more frequent during nighttime than daytime and reaches up to -0.5°C/10m (Figs. 6c and 7c).

The remaining predictors (distance from the city centre and fraction covered by buildings and by the three vegetation categories) have almost constant qualitative thermal effects, since the sign of their regression coefficient is the same at least 90% of the time (Table 3, Fig. 6d-h). Air temperature increases towards the city centre, together with the fraction of buildings (Fig. 7d-e). By contrast, air temperature decreases as the fraction covered by vegetation increases (Fig. 7f-h). The thermal effects of the distance from the city centre and land cover tend to be stronger during the night (Fig. 7d-h), i.e. when the UHI is the strongest (Richard et al. 2021) and wind speed the lowest (Fig. 3d). The remaining 10% (reversal in the sign of the regression coefficient) mostly occur just after sunrise (Fig. 6d-h) and denote weak drop shadows in the study area more than land cover effects, hence positive (negative) regression coefficients for distance from the city centre and the fraction covered by the three vegetation categories (fraction covered by buildings).

3.2 Combined effects

Combined effects are assessed by analysing the results from the MLR models built for each hour of the period 2014–2021, and using a maximum of five predictors among those listed in Table 1.

3.2.1 Mean model skill

Figure 8 shows the RMSE and R2-Adj of the MLR models averaged for the period 2014–2021 over both the diurnal and annual cycles. The RMSE metric depicts the same pattern as for SLR models, but errors are much lower (Fig. 8a compared to Fig. 4). They reach up to ~ 0.6°C at night and ~ 0.4°C during the day, with the largest errors occurring from March to September (Fig. 8a). The mean spatial errors are also significantly lower in the MLR than SLR models (Fig. 8b compared to Fig. 5). They depict a strong diurnal cycle, with the lowest skill (mean R2-Adj = 0.65) found in the early morning immediately after sunrise, and the best one (mean R2-Adj = 0.8) in the evening and in the early night (Fig. 8b).

The worst RMSE and R2-Adj reach as much as 1°C at night and 0.3 in the early morning, respectively (Supplementary Fig. S5a-b). Symmetrically, the best RMSE and R2-Adj reach 0.1°C and 0.87

(Supplementary Fig. S5c-d). This indicates a large spread in MLR skill, probably linked to meteorological conditions that are not accounted for.

The better performance of MLR models to explain the space-time variability of air temperature around the agglomeration of Dijon demonstrates that it is significantly influenced by more than one factor, like elevation, landform and land cover. The following section examines when and how each predictor influences air temperature in the MLR framework.

3.2.2 Frequency of occurrence

Elevation, valley magnitude and the fraction covered by buildings are the main drivers of air temperature spatial patterns, especially from March to October. At this time, the frequency of occurrence reaches up to 35% in the late morning and early afternoon for elevation, 25% during the night for valley magnitude, and 30% during the day for the fraction covered by buildings (Fig. 9). By contrast, hump magnitude is the least frequent predictor, occurring 10% of the time at most from November to February, and 15% of the time during the morning from March to October. Since the MLR models cannot use elevation and hump magnitude as predictors at the same time to limit multicollinearity issues, we conclude that the former has an overall larger influence on air temperature patterns. The remaining predictors occur up to 20% of the time during the night, especially from October to March for the fraction covered by low vegetation and from March to October for distance from the city centre and the two remaining vegetation predictors (Fig. 9).

We now better highlight when, over the annual and diurnal cycles, each predictor influences air temperature spatial patterns, as well as the relationship between these predictors. Elevation influences air temperature all year long (Fig. 10a). Hump magnitude influences early morning air temperature from March to October (Fig. 10b), and valley magnitude influences nighttime air temperature from July to October (Fig. 10c). The largest influence of city mineral properties is found in summer and early fall (first hours of the night for distance from the city centre: Fig. 10d; late afternoon for the fraction of buildings: Fig. 10e). Vegetation categories have different influences over the year: the forests and water category mainly influences air temperature during the night in summer and early fall for (Fig. 10f), low vegetation predominates in late fall and winter (Fig. 10h) and field crops in spring and early summer (Fig. 10g). Interestingly, the influence of field crops on air temperature spatial patterns starts ~ 1 month earlier in spring and finishes ~ 1 month earlier in summer than that of forests and water. The main field crops around Dijon are wheat, rapeseed and barley (Colbach et al. 2014). They are harvested in July, leaving bare soils from August to October. Even though vegetative cycles are not explicitly accounted for, the seasonality in the occurrence of these two vegetation predictors is consistent with the observed vegetative cycle in Burgundy.

3.2.3 Thermal effects

Mean MLR-derived regression coefficients are very consistent with those derived from the SLR models in terms of sign. Elevation, valley magnitude and, to a lesser extent, hump magnitude are associated with

regression coefficients with reversed signs between night and day (Fig. 11a-c). Adiabatic gradients prevail during daytime, while thermal inversions dominate at night. For instance, the mean influence of elevation reaches as much as ~ -1°C/100 m during daytime almost all year long and ~ + 0.5°C/100 m at night from spring to autumn. The apparent weaker intensity of nocturnal thermal inversions compared to daytime adiabatic gradients conceals a “mean effect”, due to the fact that both adiabatic gradients and thermal inversions can occur at night, while adiabatic gradients are nearly systematic during the day.

For the remaining predictors, air temperatures increase systematically towards the city centre and where the fraction covered by buildings increases, especially at night (Fig. 11d-e). The largest influence of these two predictors is found from spring to autumn, also corresponding to their most frequent occurrence (Fig. 10d-e). While the fraction of buildings is more rarely selected as a predictor during nighttime (Fig. 10e), it promotes much more intense warming than in daytime (Fig. 11e). In contrast with urban predictors, vegetation predictors mostly contribute to cool air temperatures at night (Fig. 11f-h). The only exception concerns low vegetation in the early morning in late summer, which tends to promote warmer conditions. Such a warming effect of low vegetation (and, to a lesser extent, of field crops) during the early morning may relate to the fact that low vegetation is generally located over flat and open land with no cast shadows, which therefore warms quickly after sunrise.

4. Conclusion And Discussion

This paper examines the individual and combined influences of topography (elevation and landform: hump and valley magnitude), land cover (fraction covered by buildings, low vegetation, field crops and forests and water) and urban morphology (distance from the city centre) on air temperature space-time variability measured by a dense in-situ network, in a middle-size city (Dijon, North-Est France) surrounded by contrasted topography. These descriptors are used as predictors in simple and multiple linear regression (SLR and MLR) models ran for each hour of the period 2014–2021. Their individual influences are assessed through the SLR models and their combined influences through the MLR models. Both are examined along the annual and diurnal cycles by analysing to extent to which these linear models capture the area-averaged intensity (RMSE) and spatial patterns (R2 or R2-Adj) of observed air temperature, as well as the frequency of occurrence and thermal effects of the predictors objectively selected to build them.

The analysis of individual influence reveals a complementary influence of topography and land cover on air temperature space-time variability. Thus, accounting for the combined influence of topography and land cover in the MLR models significantly improves air temperature area-averaged magnitude and spatial patterns compared to observations, especially during the day and early night.

Topography influences air temperature all year long for elevation, in the early morning from March to October for hump magnitude and during nighttime from July to October for valley magnitude. Topography is associated with almost systematic adiabatic gradients during daytime and frequent (up to 30% of the time) thermal inversions during nighttime. Such a diurnal reversal in the thermal effect of

topography is in line with what is found in urban environments with contrasted topography (Nkemdirim 1980; Goldreich 1984; Bokwa et al. 2015). Impervious surfaces are more influential in summer and early fall, especially in late afternoon for the fraction covered by buildings and in early night for distance from the city centre. They contribute to warm air temperature towards the city centre or where the fraction covered by buildings increases. Vegetation contributes to cool air temperature at night with complementary influences of the three vegetation categories over the annual cycle (low vegetation: late fall and winter; fields crops: spring and early summer; forests and water: summer and early fall). The only exception concerns low vegetation at sunrise during summer, which contributes to increase air temperatures in our MLR models. However, we have limited confidence in this warming effect, since observations associated with a large fraction of low vegetation are essentially located at the foot of hill slopes oriented from north-east to south-west, and are thus well exposed to insolation at sunrise. The thermal effects of land cover found in Dijon are in line with previous works and consistent with the well-known drivers of UHI (e.g., Eliasson 1996; Sun et al. 2009; Sun 2011; Heusinkveld et al. 2014; Song et al. 2014; Stewart 2019).

These SLR and MLR models are not perfect by any means. They struggle in capturing air temperature patterns at night and early in the morning when observed air temperature tends to be noisy spatially. Such difficulties are also found in other cities using different statistical models (e.g., Nikoloudakis et al. 2020). More sophisticated approaches may slightly improve upon our MLR approach (e.g., Szymanowski and Kryza 2009; Ho et al. 2014; Schneider Dos Santos 2020). For instance, Gardes et al. (2020) found very slight improvements with the Random Forest algorithm compared to MLR in predicting UHI over 42 French cities. The predictors themselves remain the most critical levers for improvement. The fact that the predictors used are constant in time does not seem to be a major source of error, as suggested, for example, by realistic annual cycle in the frequency of occurrence of the three vegetation categories (low vegetation, field crops and forests and water) compared to the observed vegetative cycle in Burgundy. The main source of improvement would be the inclusion of physically-based descriptors, such as sensible and latent heat fluxes, insolation or cloudiness, atmospheric stability and circulation and soil moisture. Including such physical processes would require observations or reanalyses for the entire 2014–2021 period at a sufficiently high resolution to account for spatial heterogeneity within the study area. The state of available data is not yet quite there, making it difficult to account for physical processes at this time. Similarly, we did not include the sky view factor at this stage to focus on mesoscale drivers of temperature patterns. Yet, the sky view factor may help improve the SLR/MLR skill in capturing air temperature spatial variability associated with UHI (Dirksen et al. 2019) and during the early morning, even though its physical meaning is questionable at mesoscale.

Our SLR/MLR framework proves to be a low-cost, efficient and replicable way to understand the individual and combined influences of topography and land cover on air temperature space-time variability. While applied here to an urban environment, it can easily be transposed to other environments, such as viticultural environment to understand the high space-time variability in air temperature during spring frost events.

Declarations

Acknowledgments

We are grateful to Météo-France for providing weather parameters from the Longvic station. Calculations were performed using HPC resources from PSIUN-CCUB, Université de Bourgogne Franche-Comté.

Ethical Approval

Not applicable.

Competing interests

The authors declare that they have no known competing financial interests or personal relationships that could have appeared to influence the work reported in this paper.

Authors' contributions

J.C., Y.R., B.P. and J.E. wrote the main manuscript text. J.C. and J.E. prepared the figures. Y.R., B.P. and T.T. acquired the funding. D.R. and J.D. prepared the land use dataset. J.P and M.R. prepared the temperature dataset. All authors reviewed the manuscript.

Funding

This work is a contribution to the RESPONSE programme (ERC H2020 Grant #957751: https://h2020response.eu/).

Availability of data and materials

The data and materials for this study will be made available to any individual or organization on reasonable requests via julien.cretat@u-bourgogne.fr or yves.richard@u-bourgogne.fr.

References

1. Alcoforado M-J, Andrade H (2006) Nocturnal urban heat island in Lisbon (Portugal): main features and modelling attempts. Theor Appl Climatol 84:151–159. https://doi.org/10.1007/s00704-005-0152-1
2. Arnds D, Böhner J, Bechtel B (2017) Spatio-temporal variance and meteorological drivers of the urban heat island in a European city. Theor Appl Climatol 128:43–61. https://doi.org/10.1007/s00704-015-1687-4
3. Bannari A, Teillet P, Leckie D, Fedosejevs G (2000) Impact des conditions internes et externes aux couverts forestiers sur les indices spectraux dérivés de simulations spectrales de AVHRR. Télédétection 1:151–181. https://doi.org/10.17184/eac.10287736v1n3

4. Bocher E, Petit G, Bernard J, Palominos S (2018) A geoprocessing framework to compute urban indicators: The MApUCE tools chain. Urban Climate 24:153–174. https://doi.org/10.1016/j.uclim.2018.01.008
5. Bokwa A, Hajto MJ, Walawender JP, Szymanowski M (2015) Influence of diversified relief on the urban heat island in the city of Kraków, Poland. Theor Appl Climatol 122:365–382. https://doi.org/10.1007/s00704-015-1577-9
6. Colbach N, Biju-Duval L, Gardarin A, et al (2014) The role of models for multicriteria evaluation and multiobjective design of cropping systems for managing weeds. Weed Research 54:541–555. https://doi.org/10.1111/wre.12112
7. Coseo P, Larsen L (2014) How factors of land use/land cover, building configuration, and adjacent heat sources and sinks explain Urban Heat Islands in Chicago. Landscape and Urban Planning 125:117–129. https://doi.org/10.1016/j.landurbplan.2014.02.019
8. Craney TA, Surles JG (2002) Model-Dependent Variance Inflation Factor Cutoff Values. Quality Engineering 14:391–403. https://doi.org/10.1081/QEN-120001878
9. Dirksen M, Ronda RJ, Theeuwes NE, Pagani GA (2019) Sky view factor calculations and its application in urban heat island studies. Urban Climate 30:100498. https://doi.org/10.1016/j.uclim.2019.100498
10. Edmondson JL, Stott I, Davies ZG, et al (2016) Soil surface temperatures reveal moderation of the urban heat island effect by trees and shrubs. Sci Rep 6:33708. https://doi.org/10.1038/srep33708
11. Eliasson I (1996) Urban nocturnal temperatures, street geometry and land use. Atmospheric Environment 30:379–392. https://doi.org/10.1016/1352-2310(95)00033-X
12. Emery J, Pohl B, Crétat J, et al (2021) How local climate zones influence urban air temperature: Measurements by bicycle in Dijon, France. Urban Climate 40:101017. https://doi.org/10.1016/j.uclim.2021.101017
13. Fenner D, Meier F, Scherer D, Polze A (2014) Spatial and temporal air temperature variability in Berlin, Germany, during the years 2001–2010. Urban Climate 10:308–331. https://doi.org/10.1016/j.uclim.2014.02.004
14. Foissard X, Dubreuil V, Quénol H (2019) Defining scales of the land use effect to map the urban heat island in a mid-size European city: Rennes (France). Urban Climate 29:100490. https://doi.org/10.1016/j.uclim.2019.100490
15. Fouillet A, Rey G, Laurent F, et al (2006) Excess mortality related to the August 2003 heat wave in France. Int Arch Occup Environ Health 80:16–24. https://doi.org/10.1007/s00420-006-0089-4
16. Gabriel KMA, Endlicher WR (2011) Urban and rural mortality rates during heat waves in Berlin and Brandenburg, Germany. Environmental Pollution 159:2044–2050. https://doi.org/10.1016/j.envpol.2011.01.016
17. Gardes T, Schoetter R, Hidalgo J, et al (2020) Statistical prediction of the nocturnal urban heat island intensity based on urban morphology and geographical factors - An investigation based on

numerical model results for a large ensemble of French cities. Science of The Total Environment 737:139253. https://doi.org/10.1016/j.scitotenv.2020.139253

18. Geiger R, Aron RH, Todhunter P (2003) The Climate Near the Ground, 6th Edition. Rowman & Littlefield, Lanham
19. Goldreich Y (1984) Urban topoclimatology. Progress in Physical Geography: Earth and Environment 8:336–364. https://doi.org/10.1177/030913338400800302
20. Hart MA, Sailor DJ (2009) Quantifying the influence of land-use and surface characteristics on spatial variability in the urban heat island. Theor Appl Climatol 95:397–406. https://doi.org/10.1007/s00704-008-0017-5
21. Heusinkveld BG, Steeneveld GJ, Hove LWA van, et al (2014) Spatial variability of the Rotterdam urban heat island as influenced by urban land use. Journal of Geophysical Research: Atmospheres 119:677–692. https://doi.org/10.1002/2012JD019399
22. Hidalgo J, Masson V, Gimeno L (2010) Scaling the Daytime Urban Heat Island and Urban-Breeze Circulation. Journal of Applied Meteorology and Climatology 49:889–901. https://doi.org/10.1175/2009JAMC2195.1
23. Ho HC, Knudby A, Sirovyak P, et al (2014) Mapping maximum urban air temperature on hot summer days. Remote Sensing of Environment 154:38–45. https://doi.org/10.1016/j.rse.2014.08.012
24. Hoffmann P, Schlünzen KH (2013) Weather Pattern Classification to Represent the Urban Heat Island in Present and Future Climate. Journal of Applied Meteorology and Climatology 52:2699–2714. https://doi.org/10.1175/JAMC-D-12-065.1
25. Imhoff ML, Zhang P, Wolfe RE, Bounoua L (2010) Remote sensing of the urban heat island effect across biomes in the continental USA. Remote Sensing of Environment 114:504–513. https://doi.org/10.1016/j.rse.2009.10.008
26. James G, Witten D, Hastie T, Tibshirani R (2017) An introduction to statistical learning: with applications in R, Corrected at 8th printing. Springer, New York Heidelberg Dordrecht London
27. Johnson GT, Oke TR, Lyons TJ, et al (1991) Simulation of surface urban heat islands under 'IDEAL' conditions at night part 1: Theory and tests against field data. Boundary-Layer Meteorol 56:275–294. https://doi.org/10.1007/BF00120424
28. Joly D, Bois B, Zaksek K (2012) Rank-Ordering of Topographic Variables Correlated with Temperature. Atmospheric and Climate Sciences 2:139–147. https://doi.org/10.4236/acs.2012.22015
29. Joly D, Brossard T, Cardot H, et al (2010) Les types de climats en France, une construction spatiale. Cybergeo : European Journal of Geography. https://doi.org/10.4000/cybergeo.23155
30. Jusuf S, Wong NH, Hagen E, et al (2007) The influence of land use on the urban heat island in Singapore. Habitat International 31:232–242. https://doi.org/10.1016/j.habitatint.2007.02.006
31. Kuttler W, Barlag A-B, Robmann F (1996) Study of the thermal structure of a town in a narrow valley. Atmospheric Environment 30:365–378. https://doi.org/10.1016/1352-2310(94)00271-1

32. Li X, Zhou Y, Yu S, et al (2019) Urban heat island impacts on building energy consumption: A review of approaches and findings. Energy 174:407–419. https://doi.org/10.1016/j.energy.2019.02.183
33. Macintyre HelenL, Heaviside C, Cai X, Phalkey R (2021) The winter urban heat island: Impacts on cold-related mortality in a highly urbanized European region for present and future climate. Environment International 154:106530. https://doi.org/10.1016/j.envint.2021.106530
34. Marteau R, Richard Y, Pohl B, et al (2015) High-resolution rainfall variability simulated by the WRF RCM: application to eastern France. Clim Dyn 44:1093–1107. https://doi.org/10.1007/s00382-014-2125-5
35. Matzarakis A, De Rocco M, Najjar G (2009) Thermal bioclimate in Strasbourg - the 2003 heat wave. Theor Appl Climatol 98:209–220. https://doi.org/10.1007/s00704-009-0102-4
36. Mestayer PG, Durand P, Augustin P, et al (2005) The urban boundary-layer field campaign in marseille (ubl/clu-escompte): set-up and first results. Boundary-Layer Meteorology 114:315–365. https://doi.org/10.1007/s10546-004-9241-4
37. Morris CJG, Simmonds I, Plummer N (2001) Quantification of the Influences of Wind and Cloud on the Nocturnal Urban Heat Island of a Large City. Journal of Applied Meteorology (1988-2005) 40:169–182
38. Nikoloudakis N, Stagakis S, Mitraka Z, et al (2020) Spatial interpolation of urban air temperatures using satellite-derived predictors. Theor Appl Climatol 141:657–672. https://doi.org/10.1007/s00704-020-03230-3
39. Nkemdirim LC (1980) Cold air drainage and temperature fields in an urban environment: A case study of topographical influence on climate. Atmospheric Environment (1967) 14:375–381. https://doi.org/10.1016/0004-6981(80)90071-2
40. Oke TR (1984) Towards a prescription for the greater use of climatic principles in settlement planning. Energy and Buildings 7:1–10. https://doi.org/10.1016/0378-7788(84)90040-9
41. Oke TR (1973) City size and the urban heat island. Atmospheric Environment (1967) 7:769–779. https://doi.org/10.1016/0004-6981(73)90140-6
42. Oke TR (1982) The energetic basis of the urban heat island. Quarterly Journal of the Royal Meteorological Society 108:1–24
43. Oke TR (2006) Towards better scientific communication in urban climate. Theor Appl Climatol 84:179–190. https://doi.org/10.1007/s00704-005-0153-0
44. Oke TR, Maxwell GB (1975) Urban heat island dynamics in Montreal and Vancouver. Atmospheric Environment (1967) 9:191–200. https://doi.org/10.1016/0004-6981(75)90067-0
45. Oke TR, Mills G, Christen A, Voogt JA (2017) Urban Climates. Cambridge University Press, Cambridge
46. Pascal M, Wagner V, Corso M, et al (2018) Heat and cold related-mortality in 18 French cities. Environment International 121:189–198. https://doi.org/10.1016/j.envint.2018.08.049
47. Peng S, Piao S, Ciais P, et al (2012) Surface Urban Heat Island Across 419 Global Big Cities. Environ Sci Technol 46:696–703. https://doi.org/10.1021/es2030438

48. Peng X, Wu W, Zheng Y, et al (2020) Correlation analysis of land surface temperature and topographic elements in Hangzhou, China. Sci Rep 10:10451. https://doi.org/10.1038/s41598-020-67423-6
49. Petralli M, Massetti L, Brandani G, Orlandini S (2014) Urban planning indicators: Useful tools to measure the effect of urbanization and vegetation on summer air temperatures. International Journal of Climatology 34:. https://doi.org/10.1002/joc.3760
50. Peucker TK, Douglas DH (1975) Detection of Surface-Specific Points by Local Parallel Processing of Discrete Terrain Elevation Data. Computer Graphics and Image Processing 4:375–387. https://doi.org/10.1016/0146-664X(75)90005-2
51. Qi J, Chehbouni A, Huete AR, et al (1994) A modified soil adjusted vegetation index. Remote Sensing of Environment 48:119–126. https://doi.org/10.1016/0034-4257(94)90134-1
52. Richard Y, Emery J, Dudek J, et al (2018) How relevant are local climate zones and urban climate zones for urban climate research? Dijon (France) as a case study. Urban Climate
53. Richard Y, Pohl B, Rega M, et al (2021) Is Urban Heat Island intensity higher during hot spells and heat waves (Dijon, France, 2014–2019)? Urban Climate 35:100747. https://doi.org/10.1016/j.uclim.2020.100747
54. Schneider Dos Santos R (2020) Estimating spatio-temporal air temperature in London (UK) using machine learning and earth observation satellite data. International Journal of Applied Earth Observation and Geoinformation 88:102066. https://doi.org/10.1016/j.jag.2020.102066
55. Song J, Du S, Feng X, Guo L (2014) The relationships between landscape compositions and land surface temperature: Quantifying their resolution sensitivity with spatial regression models. Landscape and Urban Planning 123:145–157. https://doi.org/10.1016/j.landurbplan.2013.11.014
56. Steeneveld GJ, Koopmans S, Heusinkveld BG, et al (2011) Quantifying urban heat island effects and human comfort for cities of variable size and urban morphology in the Netherlands. J Geophys Res 116:D20129. https://doi.org/10.1029/2011JD015988
57. Stewart ID (2019) Why should urban heat island researchers study history? Urban Climate 30:100484. https://doi.org/10.1016/j.uclim.2019.100484
58. Sun C-Y (2011) A street thermal environment study in summer by the mobile transect technique. Theor Appl Climatol 106:433–442. https://doi.org/10.1007/s00704-011-0444-6
59. Sun C-Y, Brazel AJ, Chow WTL, et al (2009) Desert heat island study in winter by mobile transect and remote sensing techniques. Theor Appl Climatol 98:323–335. https://doi.org/10.1007/s00704-009-0120-2
60. Szymanowski M (2005) Interactions between thermal advection in frontal zones and the urban heat island of Wrocław, Poland. Theor Appl Climatol 82:207–224. https://doi.org/10.1007/s00704-005-0135-2
61. Szymanowski M, Kryza M (2009) GIS-based techniques for urban heat island spatialization. Climate Research 38:171–187

62. Tan M, Li X (2015) Quantifying the effects of settlement size on urban heat islands in fairly uniform geographic areas. Habitat International 49:100–106. https://doi.org/10.1016/j.habitatint.2015.05.013
63. United Nations (2019) World Urbanization Prospects: The 2018 Revision (ST/ESA/SER.A/421). United Nations, New York
64. Wang Z, Meng Q, Allam M, et al (2021) Environmental and anthropogenic drivers of surface urban heat island intensity: A case-study in the Yangtze River Delta, China. Ecological Indicators 128:107845. https://doi.org/10.1016/j.ecolind.2021.107845
65. Whiteman CD, Haiden T, Pospichal B, et al (2004) Minimum Temperatures, Diurnal Temperature Ranges, and Temperature Inversions in Limestone Sinkholes of Different Sizes and Shapes. J Appl Meteor 43:1224–1236. https://doi.org/10.1175/1520-0450(2004)043<1224:MTDTRA>2.0.CO;2
66. Wicki A, Parlow E (2017) Multiple Regression Analysis for Unmixing of Surface Temperature Data in an Urban Environment. Remote Sensing 9:684. https://doi.org/10.3390/rs9070684
67. Zhao W, Li A, Zhang Z, et al (2016) A Study on Land Surface Temperature Terrain Effect over Mountainous Area based on Landsat 8 Thermal Infrared Data. Remote Sensing Technology and Application 31:63. https://doi.org/10.11873/j.issn.1004-0323.2016.1.0063

Figures

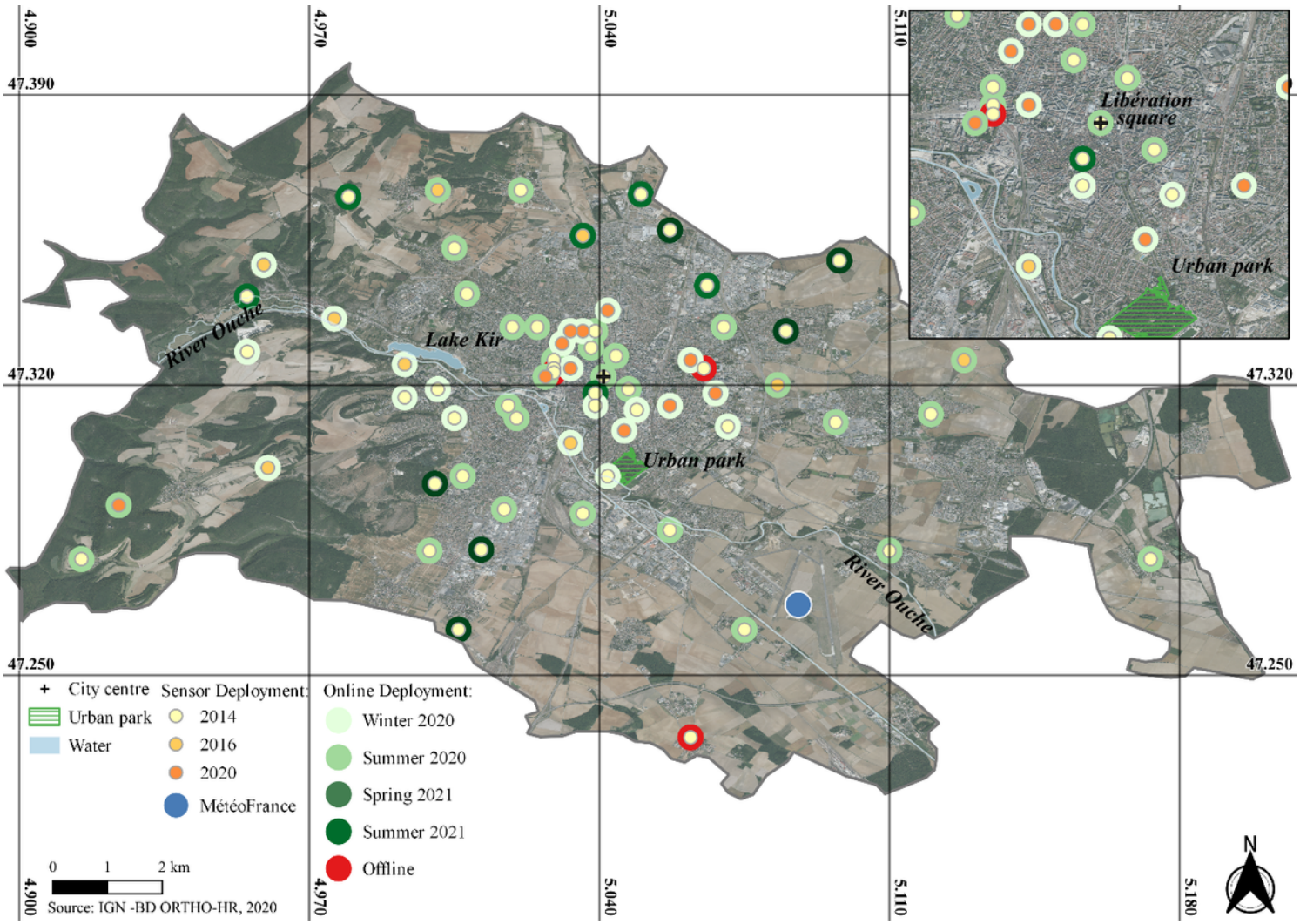


Figure 1

Location of the sensors recording hourly air temperatures in Dijon and evolution in the MUSTARDijon network from 2014 to 2021. The inset box shows the same features for the city centre. Small dots with warm colours indicate the deployment date of the sensors. Large rings with cold colours indicate the date of the changeover from manual to automatic recovery of the data. The large red dots show the stations that have been closed. The large blue dot indicates the Météo-France weather station used to describe the mean climate conditions over Dijon.

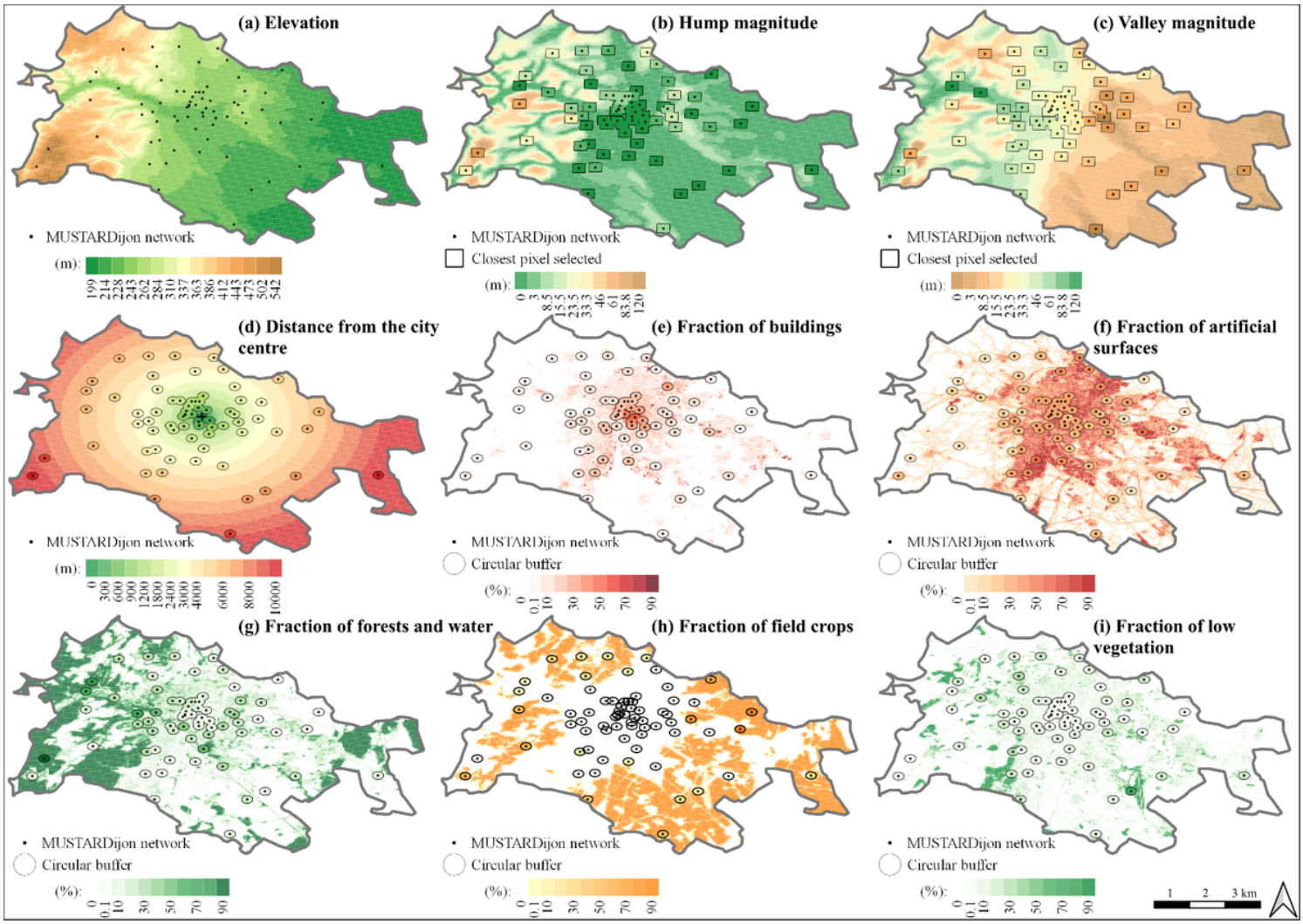


Figure 2

Topography and land cover descriptors mobilized as potential predictors in the MLR models to interpolate hourly air temperatures measured by the MUSTARDijon network in Dijon. (a-c) Topography descriptors. (d-f) Distance from the city centre and urban descriptors. (g-i) Vegetation descriptors. Circles or rectangles show the descriptor values associated with each sensor used to build the SLR and MLR models. Shading shows the descriptor values on a 100 m ´ 100 m grid covering Dijon. See the main text for details.

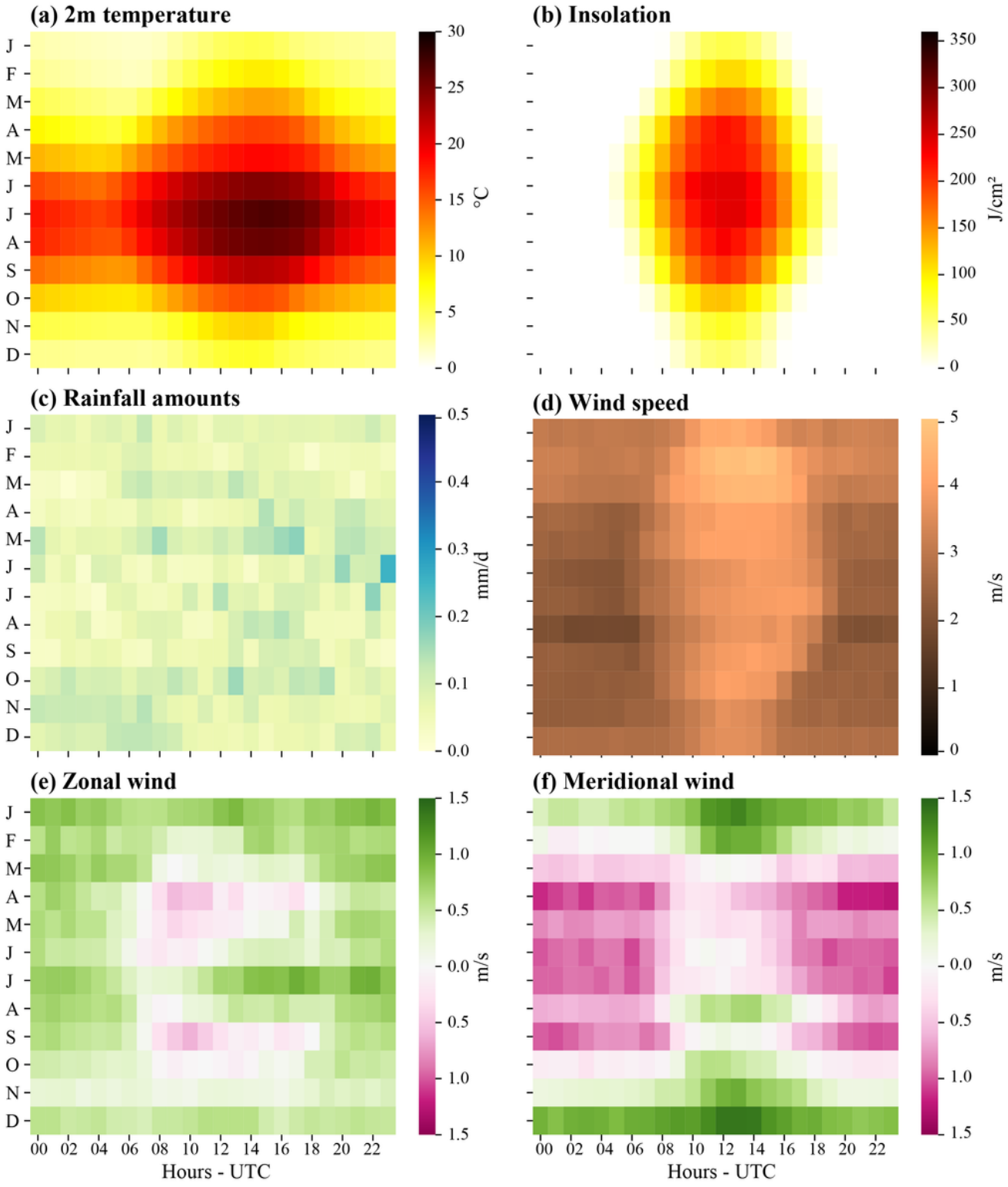


Figure 3

Hourly climatology in Dijon for the period 2014–2021. (a) 2 m temperature. (b) Insolation. (c) Rainfall amounts. (d) 10 m wind speed. (e-f) Zonal and meridional wind speed, respectively. The hourly records are measured by the Météo-France weather station located south-east of the city (blue dot in Fig. 1).

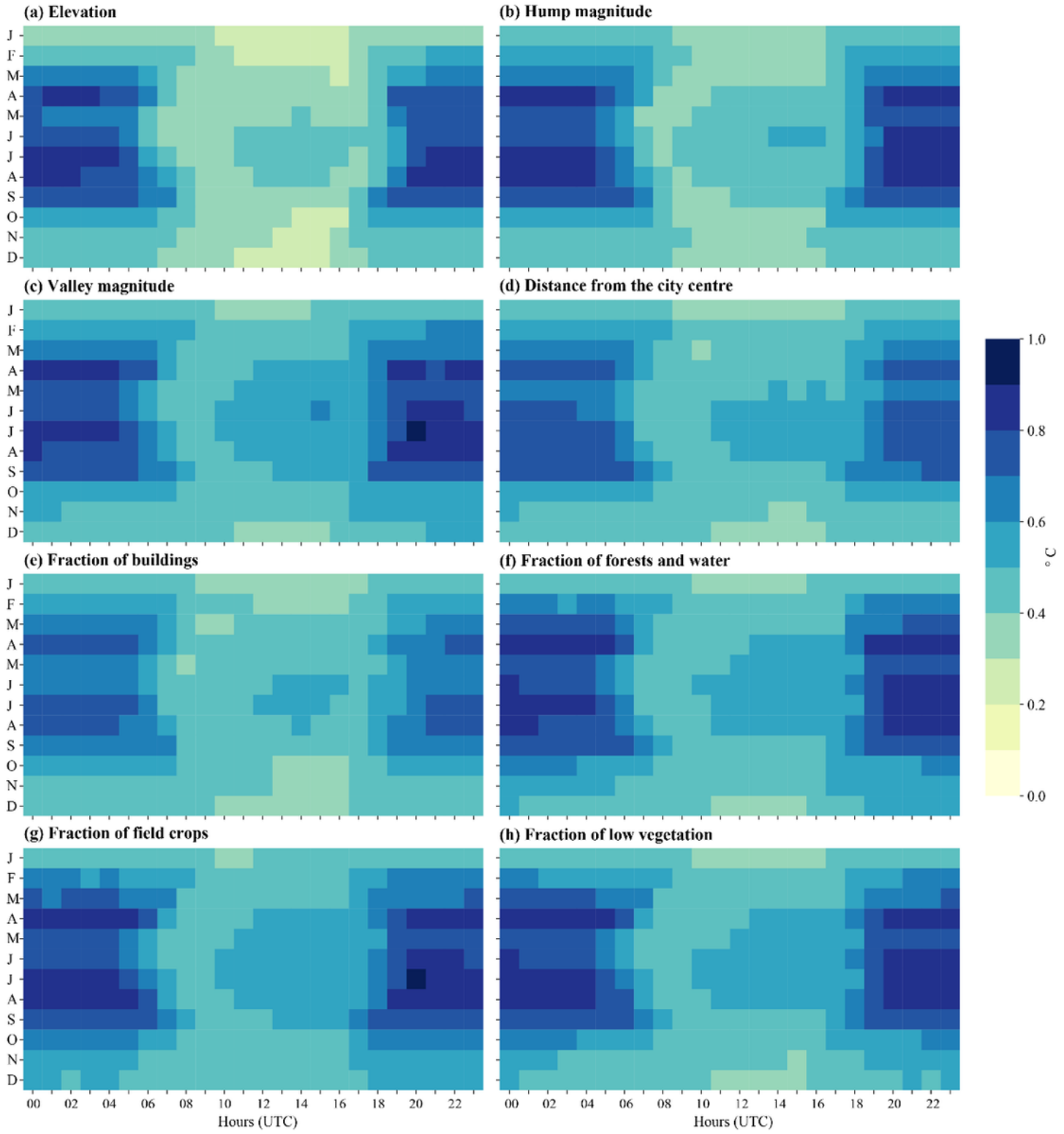


Figure 4

SLR skill in capturing the magnitude of observed air temperature over the diurnal (x-axis) and annual (y-axis) cycles for the period 2014–2021. The magnitude errors are assessed using the area-averaged RMSE obtained from LOOCV.

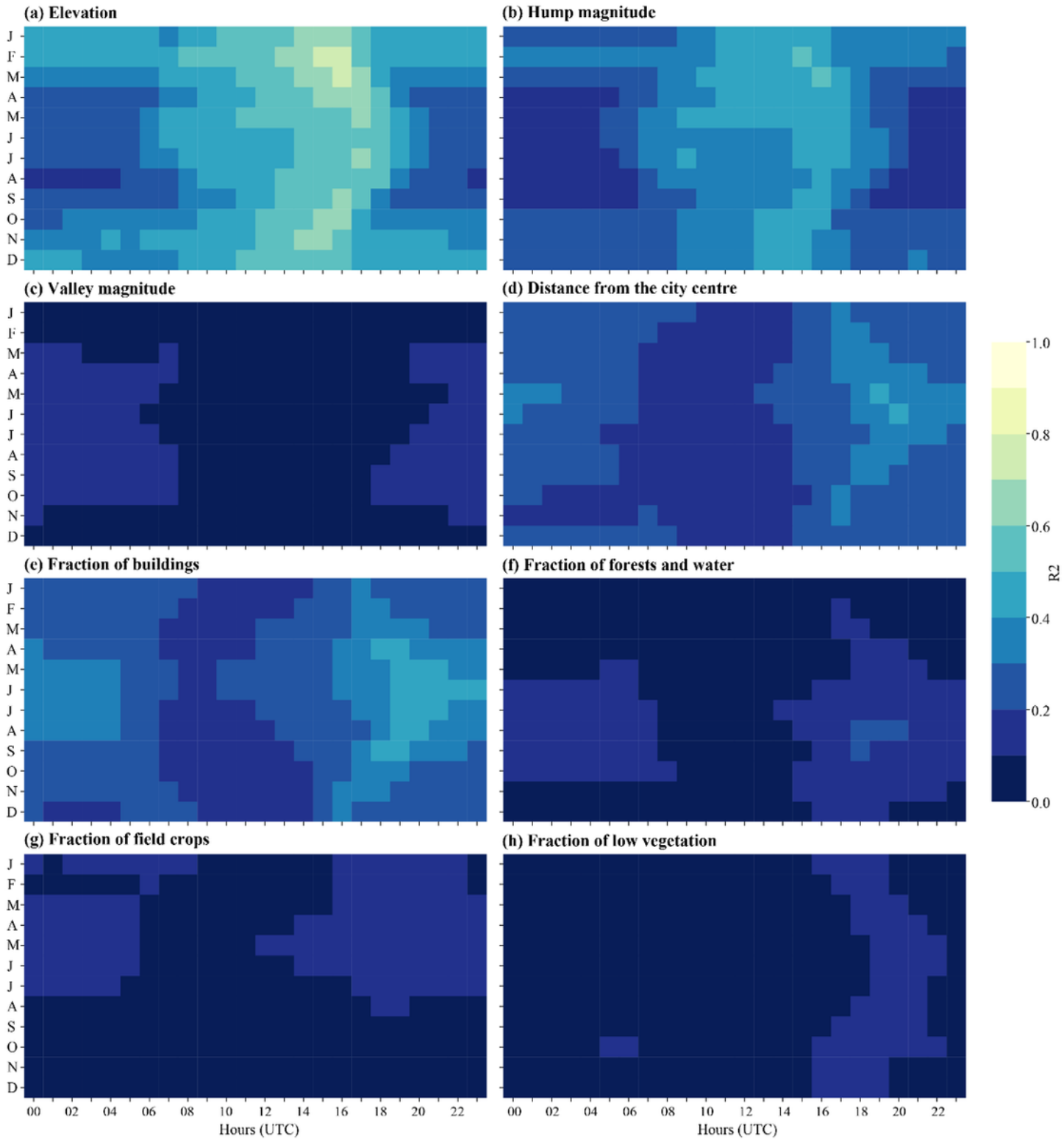


Figure 5

SLR skill in capturing the spatial patterns of observed air temperature over the diurnal (x-axis) and annual (y-axis) cycles for the period 2014–2021. The spatial pattern errors are assessed using the coefficient of determination (R2).

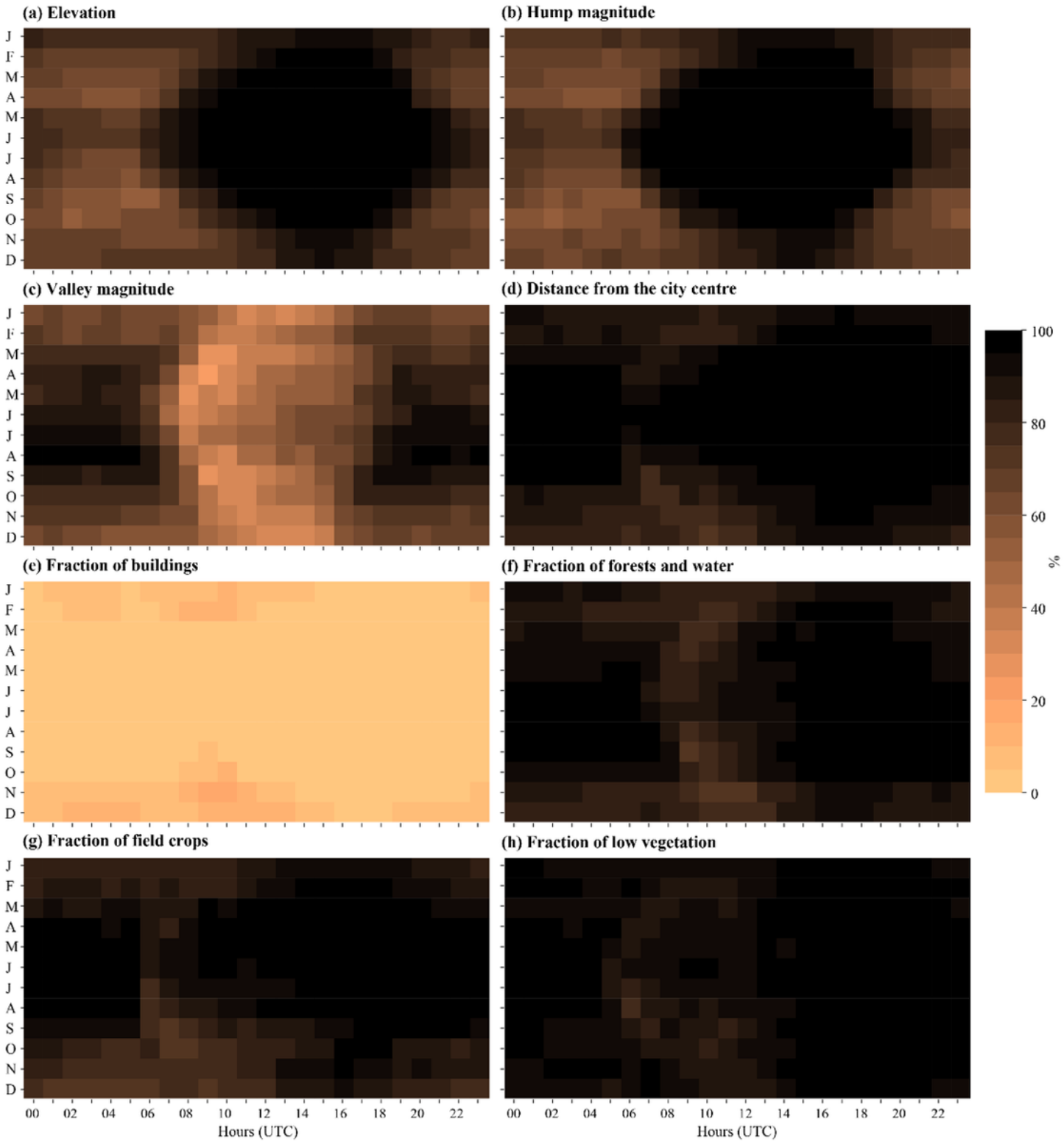


Figure 6

Frequency of occurrence of negative SLR-derived regression coefficients over the diurnal (x-axis) and annual (y-axis) cycles for the period 2014–2021.

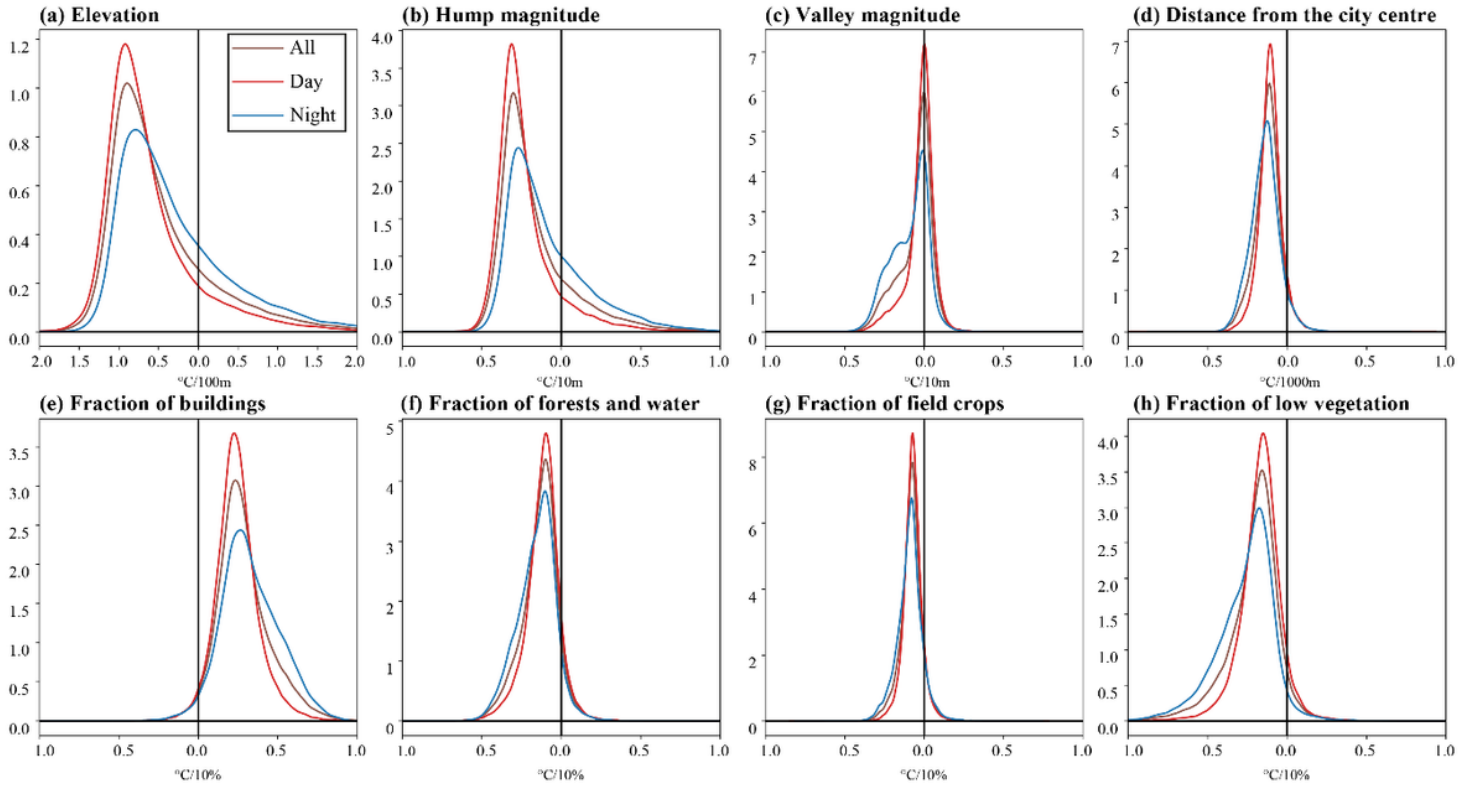


Figure 7

Probability density function of SLR-derived regression coefficients for the period 2014–2021 regardless of the diurnal cycle (All) and during daytime (Day: sunrise to sunset) and nighttime (Night: dusk to dawn of the next day).

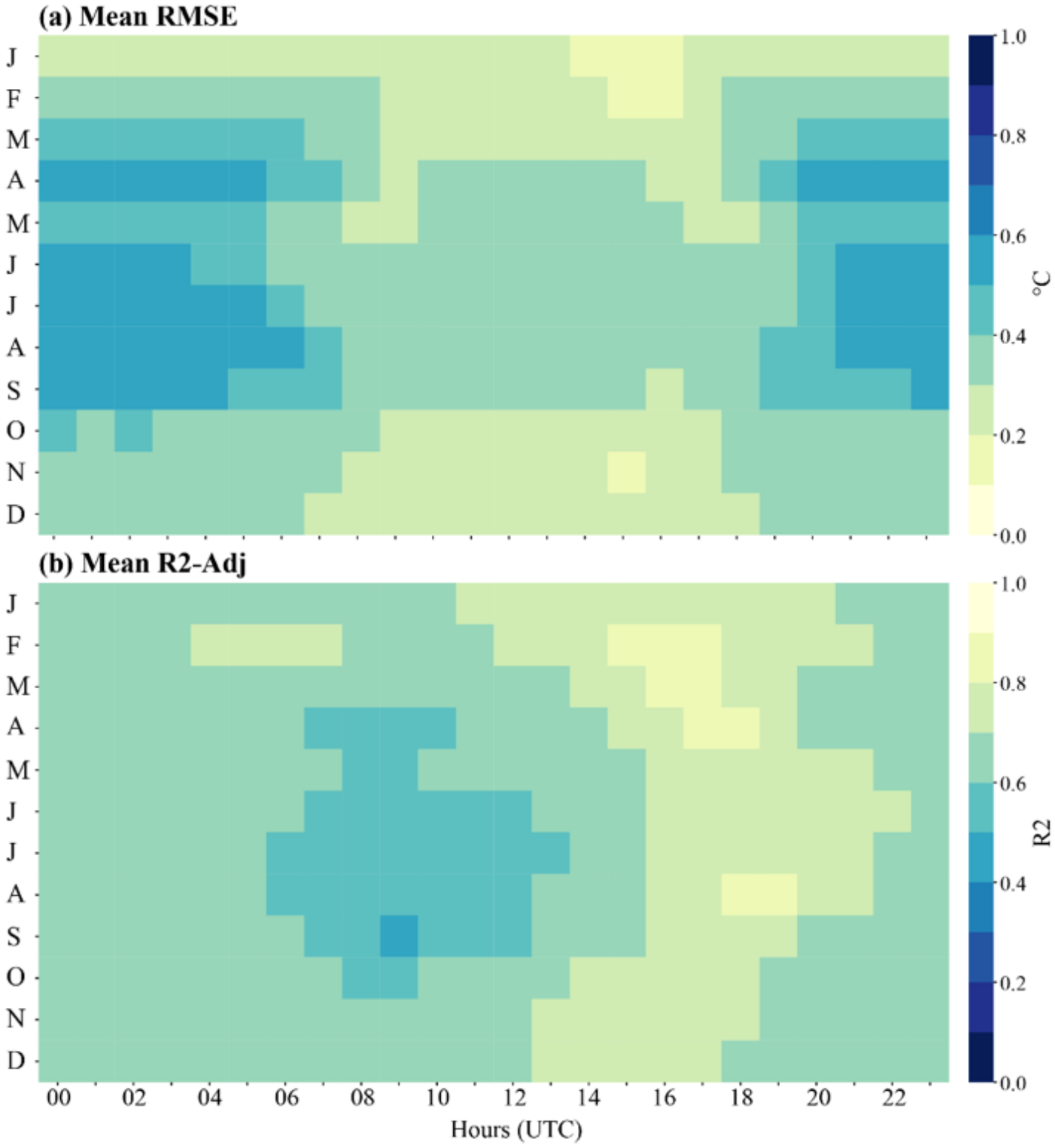


Figure 8

MLR skill over the diurnal (x-axis) and annual (y-axis) cycles for the period 2014–2021. (a) Magnitude errors as defined by area-averaged RMSE obtained from LOOCV. (b) Spatial errors as defined by the R2-Adj metric.

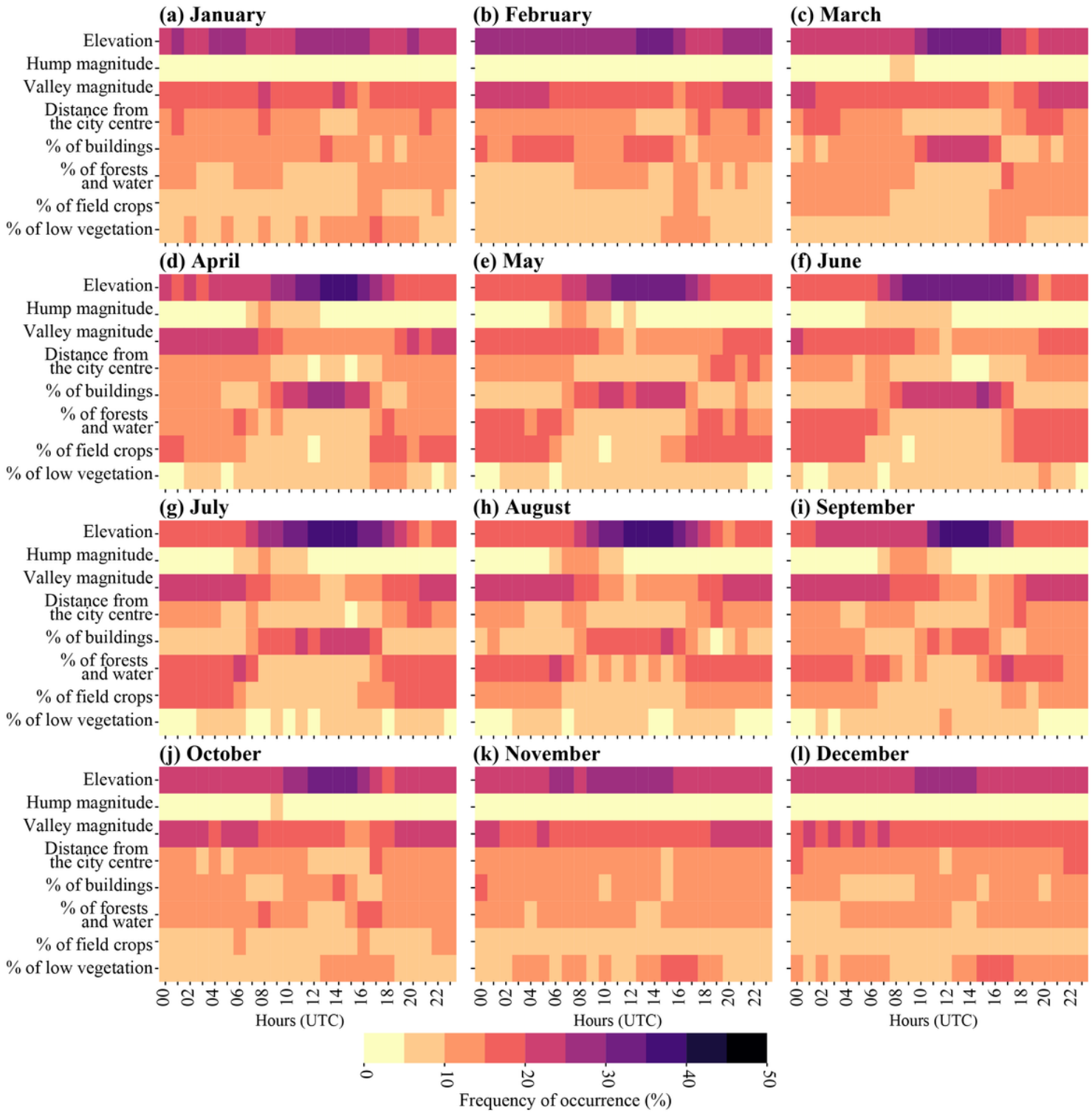


Figure 9

Frequency of occurrence of each predictor (y-axis) in the MLR models over the diurnal (x-axis) for each month for the period 2014–2021. The frequency of occurrence is defined as the ratio between the number of times each predictor is selected in the MLR models at a given hour of a given month for the period 2014–2021 (nominator) and the total number of predictors used for the same hour, month and period (denominator). For each panel, the sum of each column is 100%.

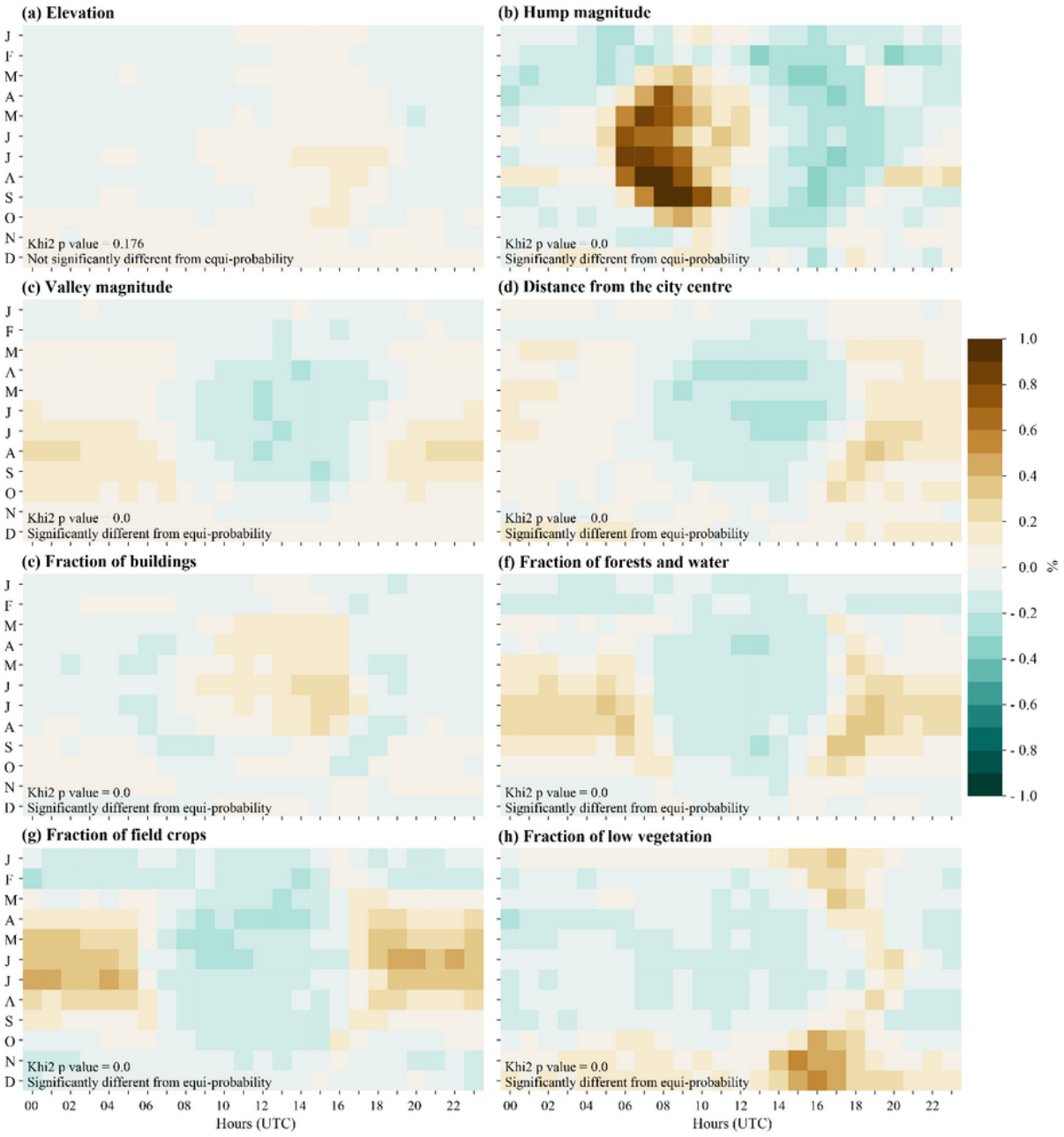


Fig. 10: Preferential occurrence of each predictor over the diurnal (x-axis) and annual (y-axis) cycles for the period 2014–2021. The preferential occurrence is defined as the difference between the frequency of occurrence of each predictor $\left(\frac{Number\ of\ occurrences\ for\ each\ hour\ and\ each\ month}{Total\ number\ of\ occurrences} \times 100\right)$ and the equiprobable frequency of occurrence $\left(\frac{1}{24\ hours \times 12\ months} \times 100\right)$. A Chi-2 test is applied to detect whether or not the frequency of occurrence of each predictor deviates significantly from equiprobable occurrence

Figure 10

See image above for figure legend

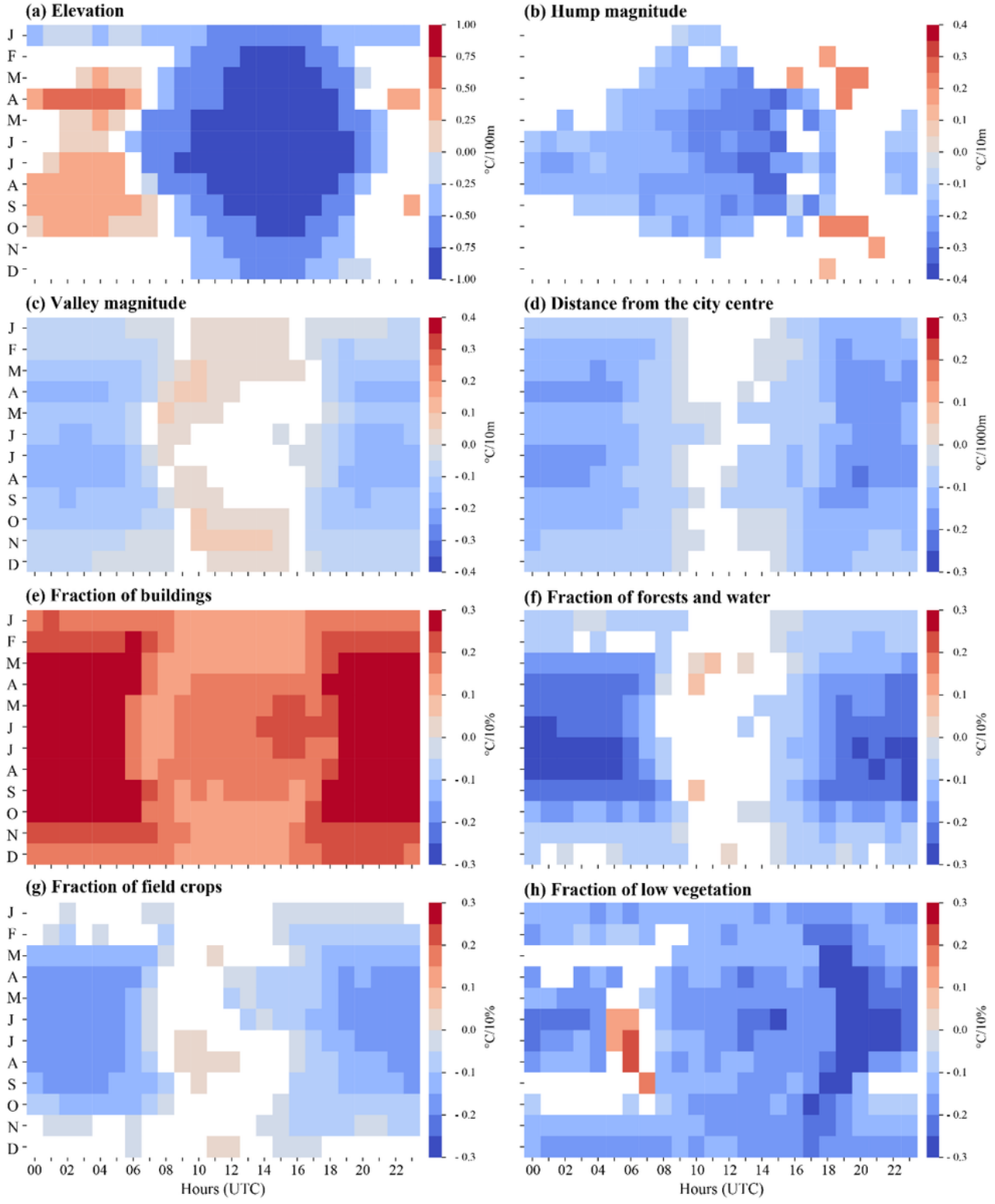


Figure 11

Mean MLR-derived regression coefficients associated with each predictor over the diurnal (x-axis) and annual (y-axis) cycles for the period 2014–2021. The mean regression coefficients are shown only when they deviate significantly from zero at the 99% confidence level according to a Student's t test.

Supplementary Files

This is a list of supplementary files associated with this preprint. Click to download.

- SI.docx